Nicotinic Acetylcholine Receptors on Osteocytes Impact Bone Mechanoadaptation in a Sexually Dimorphic Manner

Macy Mora-Antoinette[1], Mariam Obaji[2], Alexander Saffari[2], and Karl J. Lewis[2,✉]

[1]Sibley School of Mechanical and Aerospace Engineering, Cornell University, Ithaca, NY, USA
[2]Meinig School of Biomedical Engineering, Cornell University, Ithaca, NY, USA

Abstract

Bone's ability to adapt to mechanical loads is attributed the osteocyte. Osteocytes reside embedded in calcified bone matrix, where they function as the resident tissue mechanosensor. Ca^{2+} signaling is a key second messenger in mechanotransduction in osteocytes. It is used to encode mechanical load magnitude and has been linked to downstream signaling pathways which regulate bone resorbing and bone formation cell activity, however the details regarding Ca^{2+} signaling regulation in osteocytes *in vivo* are not well stratified. Osteocytes express components for nicotinic acetylcholine receptors (nAChRs) are known for calcium signaling at the neuromuscular junction. Indeed, cholinergic signaling is known to impact bone mass and fracture risk from studies in both humans and rodents. Despite this convincing evidence of the role of ACh , the details regarding cholinergic signaling in bone mechanotransduction remain largely unexplored. Here, we determine osteocytes as a functional target of cholinergic signaling for bone mechanoadaptation. We generated osteocyte-targeted conditional knockout mice for *Chrna1* or *Rapsn* using the 10kb DMP1 promotor to delete the cholinergic receptor subunit α1 and the channel grouping protein raspyn, respectively. We then performed longitudinal studies to assess skeletal morphology, tissue material make-up, and dynamic responses to anabolic challenge. Our results show sexually dimorphic differences in bone formation rates and bone structure between Cre-negative controls and conditional knockout mice. In females, the reductions to bone geometry were rescued with anabolic loading, but not in males. Our results confirm osteocytes as direct cholinergic targets with an impact on bone mechanoadaptation and suggest a direct link between bone mechanobiology and the central nervous system.

Osteocyte | Acetylcholine | Mechanoadaptation | nAChR
Correspondence: ***Karl J. Lewis, PhD: kjl235@cornell.edu***

Introduction

Bone is an exquisitely mechanically sensitive tissue, capable of adapting its bone architecture and mass to maintain a structurally sound but energetically efficient form. Harold Frost proposed that bone cells actively detect their strain environment to shape and maintain bone mass accordingly (1–3). He posited that if bone experiences prolonged periods of mechanical deformation below or above a set point value bone is resorbed or deposited, respectively. Indeed, peak healthy *in vivo* deformations for a broad range of species are tightly conserved between 0.2-0.3% (4), and applying aberrant loading at 0.2% results in anabolic bone growth in the area of maximal bending (5). In some bone metabolic diseases, the relationship between tissue deformation and bone mass becomes dysregulated. Osteoporosis, a disease characterized by the rapid loss of bone mass and increased risk of fracture, affects over 200 million people worldwide, with 1 in 3 women and 1 in 5 men projected to have a bone fragility fracture in their lifetimes (6, 7). Consequently, understanding cellular sensing mechanisms and the systems level components that regulate bone mechanotransduction are an area of critical study.

A key biological player in bone mechanotransduction is the osteocyte population. These terminally differentiated bone cells express proteins responsible for regulating the behavior of bone resorbing osteoclasts and bone building osteoblasts (8–10). They reside encased in bone matrix and are functionally connected to one another by connexin 43 gap junctions near the ends of long dendritic processes, creating a functional syncytium (11, 12). Their location throughout bone and ability to control the behavior of tissue modifying cells make them ideally designed for their role as the resident bone mechanosensors. Osteocyte mechanotransduction is a complex cell signaling event, and unraveling the critical features which serve as control mechanisms is the subject of ongoing investigation at this time.

Calcium (Ca^{2+}) signaling is a ubiquitous second messenger system with pronounced biological influence over nearly every aspect of cell function, including protein conformations, signal transduction, excitability, exocytosis, cell motility, mitochondrial integrity, apoptosis, and gene transcription (13, 14). In osteocytes, Ca^{2+} signaling is a key second messenger in mechanotransduction pathways. Activation of Ca^{2+} signaling in osteocytes *in vitro* occurs in response to fluid flow shear stress of similar magnitude to that experienced by endothelial cells (15–21) as first predicted by Weinbaum and Cowin (22). Osteocytes also exhibit increases in cytoplasmic Ca^{2+} in response to substrate deformation (23–26) and hydrostatic pressure (27–29). Moreover, osteocyte Ca^{2+} signaling is implicated in control of PGE2, RANKL, and sclerostin production (all critical regulators of bone formation and resorption) (30–39). Our group has shown that osteocytes use Ca^{2+} signaling to encode deformation magnitude (78). The variety of components and downstream effects

of Ca^{2+} signaling support the theory that it is a central control mechanism for bone mechanoregulation. As such, the mechanisms which regulate Ca^{2+} signaling dynamics in osteocytes represent important features in bone mechanotransduction. One such mechanism that has been recently implicated is acetylcholine receptors.

Cholinergic signaling is a feature of pre-ganglionic and post-ganglionic terminal autonomic nervous system function. This pathway is implicated in all organ systems; it includes the neurotransmitter acetylcholine (ACh) along with associated components for biosynthesis, signaling (e.g. transporters and receptors), and degradation (e.g. acetylcholinesterase, AChE). Neurological maladies like Alzheimer's disease are associated with the dysregulation of cholinergic activity. Interestingly, lower bone mineral density (40), higher fracture risk (41), and osteoporosis (42) are all linked to higher rates of dementia. Alzheimer's patients treated with AChE inhibitors, which increase ACh half-life, have the added benefit of reduced probability of hip fracture by 20-30% (43) along with improved hip fracture healing and microarchitectural bone quality (44). In mice, AChE inhibitors increase trabecular bone volume and reduce bone resorption (45). Parasympathetic (45) and sympathetic (46) derived ACh impact skeletal mass and development. Indeed, all three major bone cells (i.e. osteocytes, osteoblasts, and osteoclasts) express various cholinergic components (45–48). Despite this convincing evidence of the impactful role of ACh in bone biology, the details regarding cholinergic signaling in bone mechanotransduction remain largely unexplored.

Nicotinic ACh receptors (nAChRs) are ACh-gated ion channels which have high permeability to Ca^{2+} (49, 50). *Chrna1* encodes for nAChR subunit α1 of the nicotinic receptor, which binds ACh and regulates cellular activation through direct modulation of membrane potential (51, 52). Interestingly, the differentiation of osteoblasts into osteocytes is associated with upregulation of several neurotransmitter-associated genes, including *Chrna1* (47, 53). In muscle (e.g., the neuromuscular junction on mature neuromuscular synapses), α1 is involved in the of binding of ACh and channel gating to control contraction specifically through Ca^{2+} signaling (54, 55). In rat bone, *Chrna1* is downregulated after mechanical loading, indicating potential mechanical regulation of nAChRs in bone cells (53). Together, this information suggests ACh may have influence over osteocyte Ca^{2+} dynamics at the cellular level, and consequently bone mechanoadaptation at the tissue level. Rapsyn is an intracellular scaffolding proteins that tightly regulates nAChR mobility on the membrane and clusters nAChRs into functional post-synaptic groups, encoded by the gene *Rapsn* (56, 57). This cytosolic protein is critical for proper ACh signaling and highly expressed in osteocytes (47), however very little is known about its dynamics in osteocytes currently.

To date, it is not clear whether ACh induced tissue level bone architecture changes in bone result from osteocyte signaling or is mediated through some other mechanism. As such, there is a need for deeper analysis of the impacts of altered cholinergic signaling in osteocytes on bone mechanotransduction.

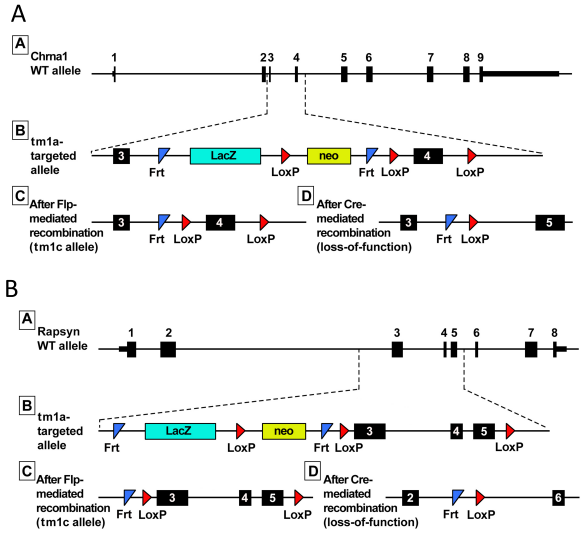

Fig. 1. Creation of *Chrna1* and *Rapsn* cKO Mouselines. Schematic showing the floxed (A) *Chrna1* and (B) *Rapsn* loci (2 exons) and the location within exon 1 of the forward and reverse primers used to probe for the intact floxed allele in genomic DNA from cortical bone.

The objective of this study was to determine if cholinergic signaling in osteocytes is relevant for bone development and mechanoadaptation. We hypothesized that cholinergic signaling in osteocytes modulates bone tissue organization and response to mechanical loading. To investigate this question, we generated osteocyte-targeted conditional knockout (cKO) mice for either *Chrna1* or *Rapsn*. We collected skeletal morphometric measurements throughout skeletal development and also after anabolic mechanical loading of bone using *in vivo* loading of the tibia. We also quantified bone matrix composition. Our results show sexually dimorphic differences in bone structure and formation rates between Cre-negative controls and cKO mice. In females, the reductions to bone geometry were rescued with anabolic loading, but not in males. Our results confirm osteocytes as direct cholinergic targets with an impact on bone mechanoadaptation and may assist in elucidating an unknown etiology to treat osteoporosis.

Methods

All procedures were approved by either the Indiana University School of Medicine or Cornell University IACUC, depending on the site of work.

Generation of *Chrna1* and *Rapsn* cKO mouse lines: *Chrna1* and *Rapsn* deletion from the mouse genome was conducted by purchasing tm1a-targeted embryonic stem cells for both *Chrna1* and *Rapsn*, from EUCOMM, which were expanded and injected into blastocysts, returned to pseudopregnant females, and screened for germline transmission in pups. Both *Chrna1* and *Rapsn* germline deletion were lethal, consistent with previous studies (58, 59), so we took steps to generate Cre-ready conditional alleles (tm1c) for both loci (Figure 1). Briefly, the correctly targeted mice harbor LacZ and Neo cassettes in intron 2 (for *Rapsn*) or 3 (for *Chrna1*) which were flanked by frt sequences. The Neo cassette was sepa-

rately flanked by loxP, and a third loxP was introduced after the final exon in the targeted sequence (exon 4 for *Chrna1* and exon 5 for *Rapsn*). To convert the tm1a allele to a tm1c conditional floxed allele, tm1a mice were crossed to Rosa26-Flp mice (Jax stock 012930; described elsewhere (60)) to induce germline recombination of the frt sites and delete the LacZ/Neo/5'loxP insert, leaving one lonely Frt site and the targeted exon(s) flanked by loxP. These tm1c mice were then crossed to the Dentin matrix protein 1 Cre (10kbDmp1-Cre; Jax stock 023047) to induce conditional deletion of *Chrna1* exon 4 or *Rapsn* exons 3-5 (both target regions house crucial exons) in osteocytes and late-stage osteoblasts. The Dmp1-Cre line has been described elsewhere (61). Both *Chrna1* and *Rapsn* lines were validated for correct targeting by long range PCR using primer pairs spanning the homology arms at both 5' and 3' ends of the targeting region. Both mutant mouse lines were on a pure C57BL/6J background. Female and male mice with Dmp1-Cre-positive conditional knockouts (cKO) in osteocytes are labeled *Chrna1*$^{\Delta Ocy/\Delta Ocy}$ and *Rapsn* $^{\Delta Ocy/\Delta Ocy}$, with littermate Dmp1-Cre-negative controls *Chrna1*$^{+/+}$ and *Rapsn* $^{+/+}$ used as the respective reference.

Dual-Energy X-Ray Absorptiometry: Bone mineral content (BMC) of the lumbar 3-5, the right leg, and the whole body was evaluated *in vivo* using dual-energy x-ray absorptiometry (DEXA). Mice were anesthetized via inhalation of 2.5% isoflurane (IsoFlo; Abbott Laboratories, North Chicago, IL) mixed with O2 (1.5 liter/min) for a total of approximately 8 min, including both induction and scanning. The mice were placed in prone position on a specimen tray within the scanner. Bone mineral density (BMD) was computed using raw bone mineral content for each region of interest. Scans were performed at 4, 6, 9, 13, 17, and 21 weeks of age. All BMC measures were normalized by body weight to eliminate the confounding effects of changing body size and weight during growth.

***In Vivo* Tibial Loading:** The axial tibial compression model was applied to Cre-positive and Cre-negative mice as previously described (62). Prior to loading, calibration mice for each sex and genotype were sacrificed at 17 weeks of age to collect strain measurements. Disarticulated hindlimbs previously stored at 20°C were used for strain gage calibration. A single-element strain gage (EA-06-015DJ-120; Vishay Precision Group, Malvern, PA, USA) was applied to the posterior midshaft surface of the tibia. The load-strain relationship was measured for each sample by applying step loading up to 11N. A load-strain curve was derived from simultaneous recording of the voltage output from the load cell and strain gage. All tests were averaged within each genotype/sex to establish a calibration curve.

For *in vivo* anabolic loading, mice were anesthetized using isoflurane inhalation and their right hindlimb (knee to foot) was loaded to a calibrated peak strain value of 2250με using a haversine waveform (2 Hz, 180 cycles). Mice were given three bouts over a 5-day period with a day of rest between each bout. Mice were sacrificed 12 days after the final bout.

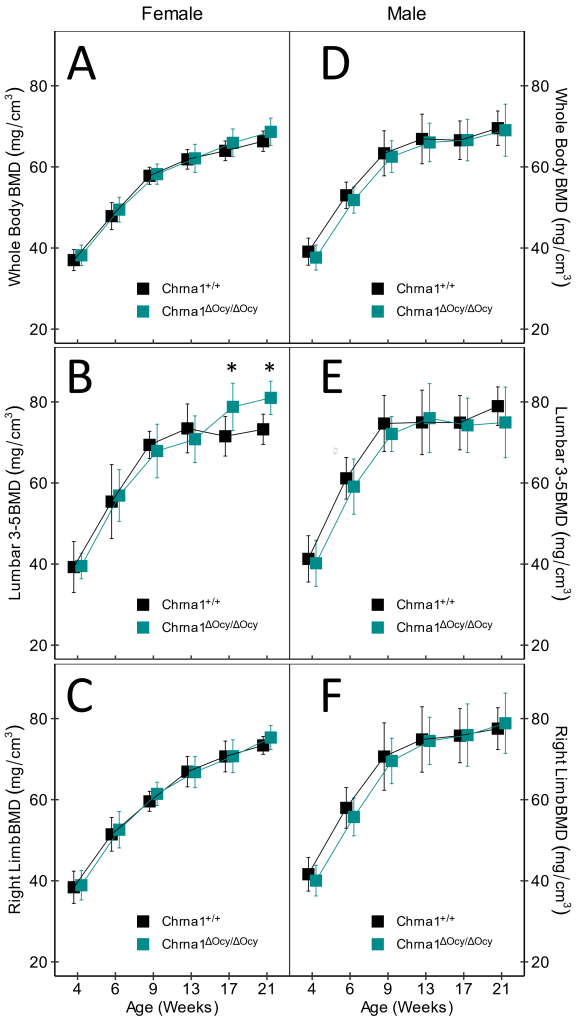

Fig. 2. *Chrna1* cKO produces normal skeletons during development and in lumbar. Raw bone mineral content was measured using DEXA and BMD was computed for the segments 3, 4, and 5 of the lumbar spine, the right limb, and the whole body between 4-21 weeks of age. (A-C) Female *Chrna1*, (D-F) Male *Chrna1*. Two-way ANOVA was performed with interactions between Genotype and Age. N = 6-15/group. A post-hoc Bonferroni test was computed across genotypes for each timepoint to determine significance (*p<0.05).

Microcomputed Tomography: Tibiae were harvested 12 days after the final bout of tibial loading, wrapped in saline soaked gauze, and stored in an airtight container at – 20°C. Geometric properties of trabecular and cortical bone were evaluated using high-resolution microcomputed tomography (µCT, Scanco Medical AG). Distal and mid-diaphysis 9µm voxel size resolution scans were imported into Scion Image version 4.0.2 (Scion Corporation), where properties were calculated using standard and customized macros. Standard measurements (77) included cortical area (mm^2), maximum (Imax, mm^4) and minimum (Imin, mm^4) cross-sectional moments of inertia, polar moment of inertia (pMOI, mm^4), total volume (TV, mm^3), bone volume (BV, mm^3), bone volume fraction (BV/TV, %), connectivity density (Conn.D, mm^{-3}), structure model index (SMI), trabecular number (Tb.N, mm^{-1}), trabecular thickness (Tb.Th, µm), and trabecular separation (Tb.Sp, µm), bone mineral content (BMC, g),

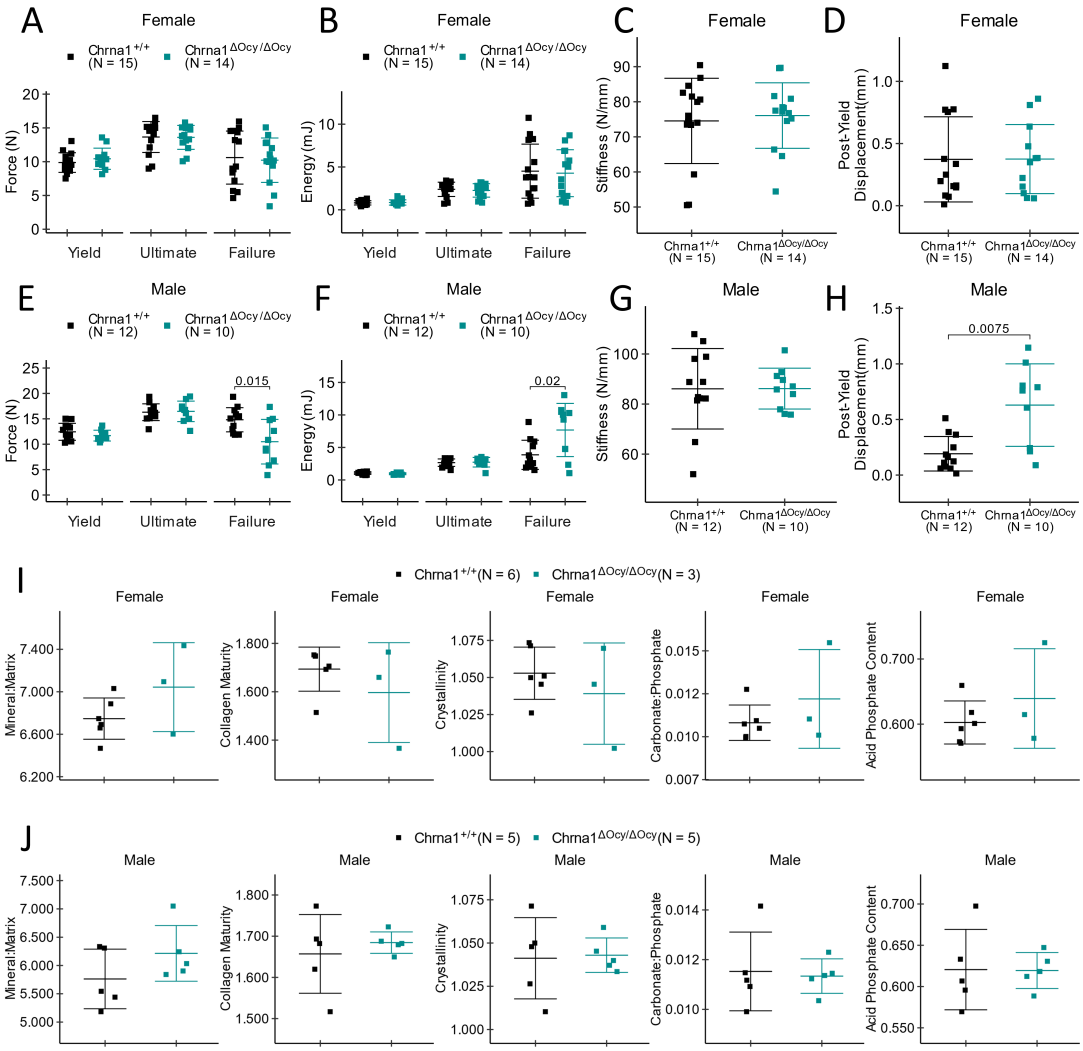

Fig. 3. *Chrna1* cKO increased femur ductility and toughness in males. Femurs were dissected for µCT to measure bone geometry of (A-D) females and (E-H) males. In addition, we performed three-point bending of right femora from 16-18 week old *Chrna1* cKOs and age-matched controls for (A-J) females and (K-T) males. Mechanical properties were computed from the load-displacement curves. FTIR was used to evaluate bone compositional properties from a subset of left femora from mice used for mechanical testing for (I) females and (J) males. Student T-tests were performed with cKO and Cre-negative controls to determine significance ($p<0.05$) for each metric.

and bone mineral density (BMD, mg/cm3).

Bone Histomorphometry: An intraperitoneal injection of calcein was given 1 day after the final bout of tibial loading, followed by an intraperitoneal injection of alizarin complexone 8 days later. Mice were sacrificed 3 days after alizarin injection. The right and left tibias were harvested and placed in 10% neutral buffered formalin for 2 days followed by storage in 70% ethanol at 4°C. Tibiae and femora were dehydrated in graded alcohols, cleared in xylene, and embedded in methyl methacrylate. To measure load-induced bone formation, thick sections were cut from the tibia approximately 3 mm proximal to the tibio-fibular junction and ground down with a polisher to approximately 50 µm (Multiprep Polishing System Allied High Tech Products). Tibial diaphysis sections were mounted unstained to visualize and read the calcein and alizarin labels administered at 17 and 18 weeks. Sections were imaged on a fluorescent microscope using filter sets that provide excitation and emission for the calcein and alizarin wavelengths. Digital images were imported into ImageJ and the following histomorphometric measurements (63, 64) were recorded for the periosteal and endosteal surfaces: total perimeter, single-label perimeter (sL.Pm), double-label perimeter (dL.Pm), interlabel thickness (Ir.L.Th), and total bone area and marrow area. The following results were calculated: mineral apposition rate (MAR = Ir.L.Th/8 days), mineralizing surface (MS/BS = (0.5 × sL.Pm + dL.Pm) / total perimeter × 100), and bone formation rate (BFR/BS = MAR × MS/BS × 3.65). Relative formation parameters for loading effects were calculated for each mouse by subtracting the non-loaded (left tibia) values from the loaded (right tibia) values.

Mechanical Testing: Mice were sacrificed at 16-18 weeks and the right femurs were harvested and stored at -20°C in saline soaked gauze until testing. On the day of testing, femurs were brought to room temperature slowly in a saline bath for over 1 hour. Femurs were positioned posterior side down across the two lower supports of a three-point bending fixture. The femurs were loaded to failure in monotonic

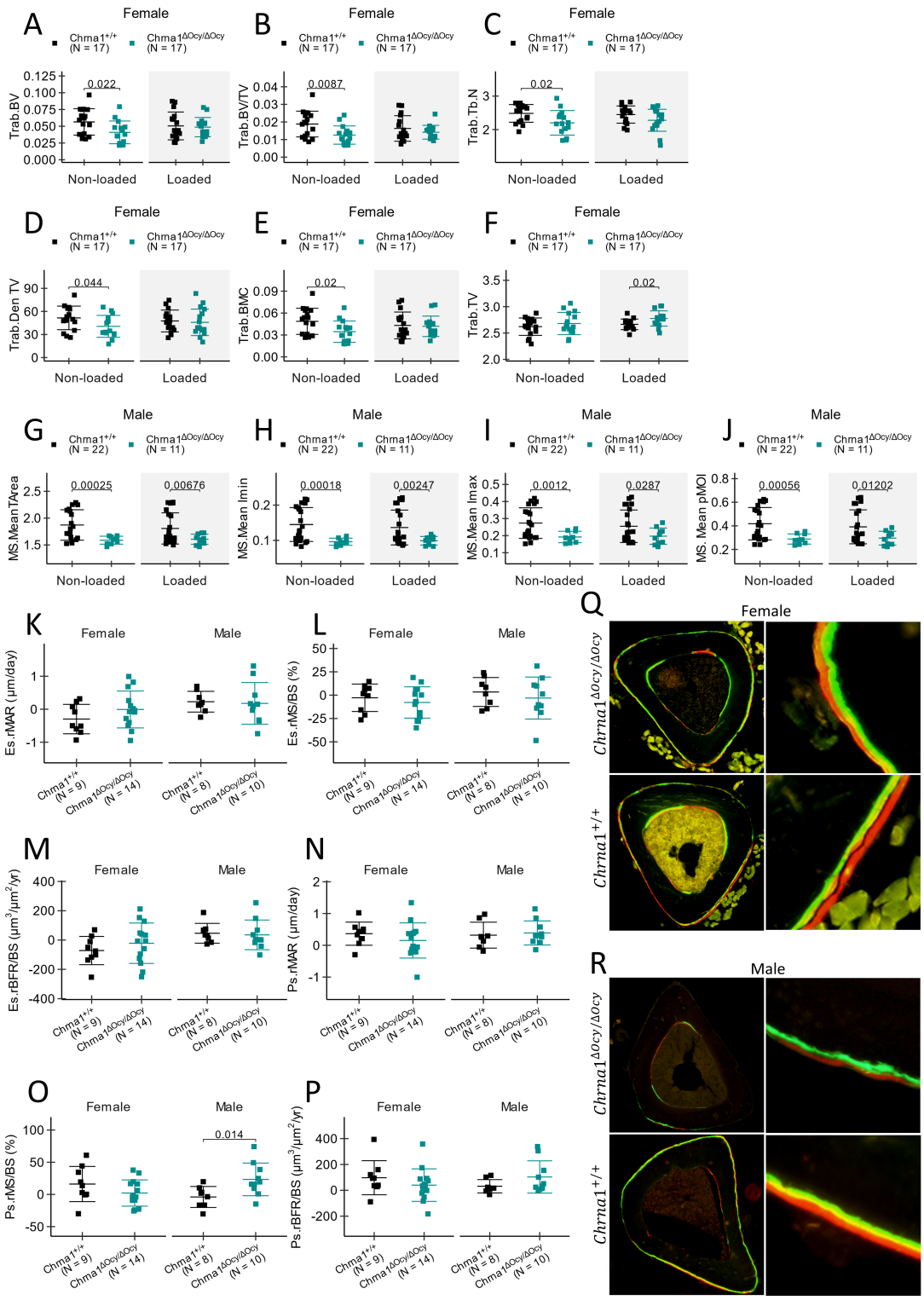

Fig. 4. *Chrna1* cKO impaired the anabolic response to mechanical loading. Adult mice were subjected to tibial loading and bones dissected 12 days later. µCT of dissected tibia measured bone geometry for (I-L) females and (M-X) males to compare loaded limbs (shaded grey background) and non-loaded limbs (white background). Female *Chrna1* cKOs exhibited differences in cortical bone volume and density and male *Chrna1* cKOs exhibited differences in trabecular and midshaft bone density. Fluorochrome labeling was used for osteoblast-derived indices of dynamic histomorphometry in (I-L) females and (O-S) males with relative metrics computed by subtracting non-loaded limbs from loaded limbs. Indices were computed for both the endosteal and periosteal surfaces. Student T-tests were performed between cKOs and Cre-negative controls to determine significance ($p<0.05$). For µCT, groups within each loading regime (i.e. non-loaded and loaded) were compared.

compression with a span length of 9mm using a crosshead speed of 0.2 mm/s using a mechanical testing system (858 Mini Bionix; MTS, Eden Prairie, MN, USA), during which force and displacement measurements were collected every 0.025s. Force and displacement measurements were measured using a 25-pound load cell (SSM-25 Transducer Tech-

niques, Temecula, CA, USA) and a linear variable differential transducer (a calibration curve spanning the expected force range was generated prior to testing). From the force versus displacement curves, ultimate force (N), ultimate energy (mJ), failure energy (mJ), stiffness (N/mm), yield force (N) and Post-Yield Displacement (PYD, mm) were calculated using standard equations (65). Prior to testing, the length of each femur was measured to the nearest 0.01 mm, along the diaphyseal axis using digital calipers.

Fourier Transform Infrared Spectroscopy: Fourier Transform Infrared Spectroscopy (FTIR) was used to evaluate bone compositional properties. Left femora from mice used for mechanical testing were harvested and stored at -20°C in saline soaked gauze until specimen preparation (66). Briefly, epiphyses of the femur was detached and bone marrow was removed using a centrifuge. The pieces were defatted in 3x-15 minute solution changes of 100% isopropyl ether. Samples were lyophilized in a vacuum drier and made into powder using a CryoMill (770; SPEX SamplePrep, Metuchen,NJ, USA). Pellets were constructed by mixing 2.0-3.0 mg of powdered bone with dry potassium bromide to make a 200mg mixture. Pellets were pressed with a 13-mm-diameter die and a maximum load of 10 tons using an evacuable pellet press (Pike Technologies, Fitchburg, WI, USA). FTIR spectra were collected at a spectral resolution of 4 cm-1 over the spectral range of 800 to 2000cm-1 using an FTIR spectrometer (Spotlight 400; Perkin-ElmerInstruments, Waltham, MA, USA). Spectra were analyzed in which areas were defined between the following peaks for Phosphate: 916-1180 cm^{-1}, Amide I: 1596-1712 cm^{-1} and Carbonate: 852-890 cm^{-1}. The peak height ratios were defined as the following Crystallinity: 1030/1020, Acid Phosphate: 1126/1096 and collagen maturity (cross-linking ratio): 1660/1690.

Whole-Mount Tissue Clearing and Immunofluorescent Staining: Mice were perfused with zinc formalin (contains 3.7% formaldehyde) and bones are dissected and fixed overnight in zinc formalin. Decalcification occurs over 5 days in 7.5pH buffered 20% EDTA at 37°C with daily solution changes and decolorized with 15% hydrogen peroxide for less than 1 hour. Immunofluorescent staining occurs before further proceeding. Samples are blocked with 10% Donkey Serum (Sigma D9663-10ML) and 3% BSA in PBST overnight. Primary antibodies are incubated at 1:100 dilution in blocking buffer for 48 hours. Primary antibodies used are Rabbit Anti-Tyrosine Hydroxylase Antibody (TH, Sigma AB152) and Goat Anti-Vesicular Acetylcholine Transporter Antibody (VAChT, Sigma ABN100). Samples are washed in PBST overnight. Secondary antibodies are then incubated at 1:200 dilution in PBST for 48 hours. Secondary antibodies used are Alexa Flour 488 donkey anti-goat antibody (Thermo Fisher Scientific A11055) and Alexa Flour 546 donkey anti-rabbit antibody (Thermo Fisher Scientific A10040). Samples go thru a final wash in PBST overnight. Tissue clearing is then finalized with dehydration in 2-ethoxyethanol for 4 hours, followed by 3 changes of acetonitrile between 4 hours or overnight at room temperature. Bones are then cleared in benzyl alcohol for 4 hours before being placed in final refractive index matching solution of benzyl benzoate (refractive index 1.5) for long term storage and imaging.

Light-Sheet Fluorescent Microscopy: Imaging of tissue cleared third metatarsals is done using a Light-Sheet microscope (LaVision BioTec) at the Cornell Institute for Biotechnology Resource Center (Cornell BRC). Bones were mounted to clear hematocrit tubes using cyanoacrylate, then the tubes were attached to a custom-made mount for the microscope. Samples were completely submerged in a container filled with refractive index matching solution (Benzyl Benzoate and any residual Benzyl Alcohol; refractive index 1.5). Imaging was performed with two channels at excitation wavelengths of 488 nm (6-8% power, emission collected with bandpass filter of 525/50) and 561 nm (9-11%, emission collected with bandpass filter 620/60) using an Olympus 2x CDC objective with a 3.5 collar and DBE correction for high RI. Two light sheets illuminate the sample from either right and left directions in series, and images are acquired with a dynamic horizontal focus processing that blends the two different images into a single image that optimally reduces the scattering compared to a single light sheet. Both light sheets are calibrated and aligned with one another in the z-plane before imaging. To image an entire bone, mosaic tiling with a 10% overlap and 1x3 tiles is used with 3.2X zoom, sheet NA 1.20, and sheet width 40%. Final pixel resolution is 0.94 x 0.94 x 4 micron. Files are saved in TIF OME format for each tile and channel, totally 6 raw data images. Images are stitched using BigStitcher in FIJI (NIH). Stitched images are converted into Imaris (Oxford Instruments) files. Channel shifting, 100 micron radius background subtraction, and 1.2 gamma correction are applied in Imaris. Finally, using the filaments tool in Imaris, large nerve fiber-like objects are manually traced and quantified using Imaris metrics.

Statistical Analysis: The effect of the cholinergic cKO on measurements of bone geometry, mineral density, mechanical properties, and metabolism were determined using a one-way ANOVA with group as the factor (Cre-negative littermate controls against Cre-positive experimental mice for the same sex) followed by unpaired one-tailed T-tests with alternative hypotheses as less than or greater than the control group depending on our hypothesis regarding the changing phenotypes. For DEXA BMD measurements, Two-way ANOVA was performed with interactions between Genotype and Age. A post-hoc Bonferroni test was computed across genotypes for each timepoint. Outliers greater than three standard deviations from the mean for each metric grouped by sex were removed. Statistical tests were conducted using R (v.3.6) with $\alpha = 0.05$.

Results

Osteocyte-targeted cholinergic disruption with *Chrna1* cKO leads to site specific skeletal abnormalities. The α1 nicotinic subunit is responsible for ACh binding during receptor activation. To assess the impact of α1 nicotinic cholinergic receptor function in osteocytes, we achieved cKO of *Chrna1* in an osteocyte-targeted manner using a

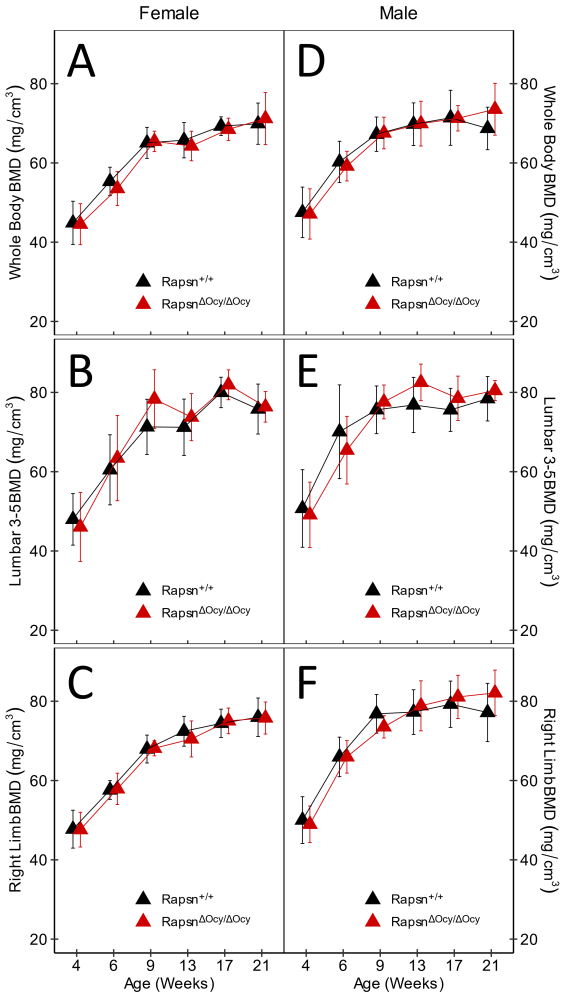

Fig. 5. *Rapsn* cKO produces normal skeletons during development and in lumbar. Raw bone mineral content was measured using DEXA and BMD was computed for the segments 3, 4, and 5 of the lumbar spine, the right limb, and the whole body between 4-21 weeks of age. (A-C) Female *Chrna1*, (D-F) Male *Chrna1*. Two-way ANOVA was performed with interactions between Genotype and Age. N = 6-15/group. A post-hoc Bonferroni test was computed across genotypes for each timepoint to determine significance (*p<0.05).

10kb DMP-1 targeted Cre-Lox system (Figure 1A). We performed sequential DEXA scans of the whole body, hind limbs, and lumbar spine in *Chrna1*$^{\Delta Ocy/\Delta Ocy}$ mice and littermate aged matched *Chrna1*$^{+/+}$ controls at intermittent periods between the ages of 4 and 21 weeks. We found that *Chrna1*$^{\Delta Ocy/\Delta Ocy}$ mice generally formed skeletons with normal BMD compared to *Chrna1*$^{+/+}$ controls (Figure 2A-F), with the only exception being in *Chrna1*$^{\Delta Ocy/\Delta Ocy}$ female mice, which exhibited increased BMD in the lumbar spine at 17 weeks (+10.6%; Figure 2B) and 21 weeks (+11.7%; Figure 2B). We also evaluated tissue level differences using µCT analysis of tibiae. In the tibia, we saw sexually dimorphic site-specific changes. *Chrna1*$^{\Delta Ocy/\Delta Ocy}$ females exhibited reduced bone mass at the metaphysis compared to *Chrna1*$^{+/+}$ mice. This included reductions in trabecular bone volume (-27.3%, Trab.BV; Figure 4A), the number of trabeculae (-10.6%, Trab.Tb.N; Figure 4C) and the bone mineral content (-29.0%, Trab.BMC; Figure 4E). This was accompanied by reductions in the ratio of bone volume to total volume (-32.7%, Trab.BV/TV; Figure 4B) and the density of total volume (-20.4%, Trab.Den TV Figure 4D). By contrast, *Chrna1*$^{\Delta Ocy/\Delta Ocy}$ males exhibited a midshaft phenotype with reduced cortical geometry. They had midshafts with lower mean total area (-15.2%, MS.MeanTArea; Figure 4G), resulting in lower minimum and maximum moment of inertias (-33.6% MS.Mean Imin and -29.7% MS.Mean Imax; Figure 4H-I, white background) and lower polar moment of inertia compared to *Chrna1*$^{+/+}$ males (-31.1%, MS.Mean pMOI, Figure 4J).

Osteocyte-targeted *Chrna1* deletion impacts toughness in male femurs. We next set out to determine if there would be changes to the whole bone mechanical properties at peak bone mass. Femurs from 16-18 week mice were subjected to monotonic three-point bending to failure. Female *Chrna1*$^{\Delta Ocy/\Delta Ocy}$ mice were not different than Cre-negative littermate controls (Figures 3A-D). Conversely, male *Chrna1*$^{\Delta Ocy/\Delta Ocy}$ mice had greater plastic deformation, indicating their bones were more ductile and resistant to mechanical failure. Male *Chrna1*$^{\Delta Ocy/\Delta Ocy}$ mice had -29.1% reduced fracture force (Figure 3E), +98.7% increased failure energy (Figure 3F) and 228% increased post-yield displacement (Figure 3G) compared to Chrna1$^{+/+}$ controls. After measuring tissue composition of a subset of femurs used for mechanical testing, we determined no changes to the mineral to matrix ratio, collagen maturity, or mineral crystallinity for cKO compared to Cre-negative controls (Figure 3I-J).

Osteocyte-targeted *Chrna1* deletion impairs bone anabolic response to mechanical challenge. To assess the impact of osteocyte cholinergic signaling on bone mechanotransduction, we studied tissue changes in response to *in vivo* loading. Mice received *in vivo* tibial loading to peak calibrated strain magnitudes of -2250με 3 times per week for 2 weeks. Post-mortem analyses of loaded and non-loaded tibia included µCT and dynamic histomorphometry. Non-loaded tibiae from *Chrna1*$^{\Delta Ocy/\Delta Ocy}$ females exhibited reduced trabecular bone mass at the metaphysis compared to Cre-negative littermate controls. This phenotype was rescued in loaded bones (Figure 4A-E, grey background), with trabecular total volume (Trab.TV; Figure 4F grey background) even exceeding that of Chrna$^{+/+}$ controls by +4.2%. Non-loaded tibiae from *Chrna1*$^{\Delta Ocy/\Delta Ocy}$ males had normal trabecular bone but exhibited a midshaft phenotype with reduced cortical geometry without loading. Unlike females, anabolic loading did not rescue the phenotype (Figure 4G-J, grey background), indicating irreversible changes to the midshaft in Chrna$^{\Delta Ocy/\Delta Ocy}$ male mice. Relative dynamic histomorphometry indices were assessed by subtracting non-loaded values from loaded limbs. In *Chrna1*$^{\Delta Ocy/\Delta Ocy}$ mice, females showed no differences compared to controls (Figure 4 K-Q). Males had enhanced mineralizing surface on the endosteum (+27.3%, Es.rMS/BS; Figure 4 O and R).

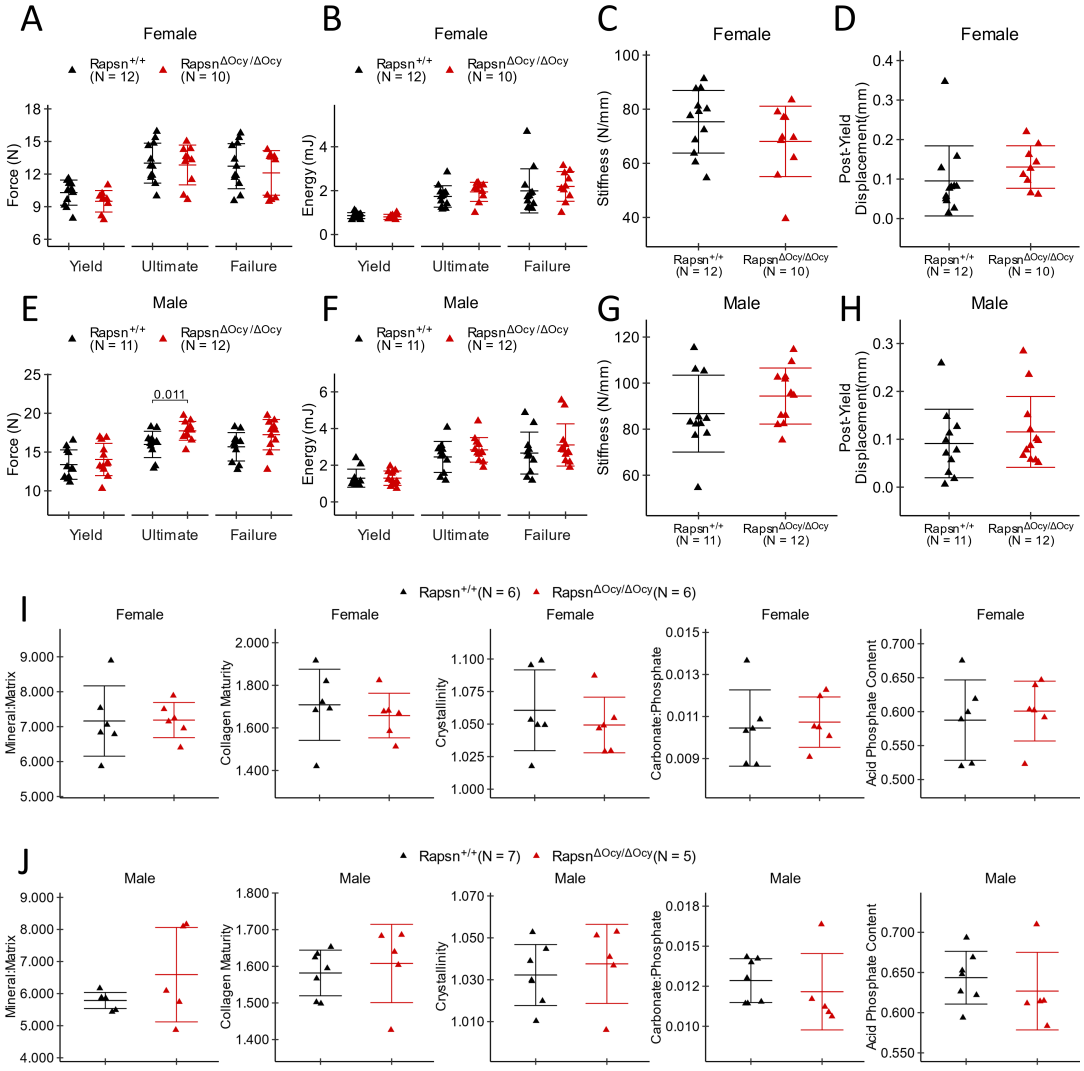

Fig. 6. *Rapsn* cKO did not alter whole bone mechanical properties. Femurs were dissected for µCT to measure bone geometry of (A-D) females and (E-H) males. In addition, we performed three-point bending of right femora from 16-18 week old *Rapsn* cKOs and age-matched controls for (A-J) females and (K-T) males. Mechanical properties were computed from the load-displacement curves. FTIR was used to evaluate bone compositional properties from a subset of left femora from mice used for mechanical testing for (I) females and (J) males. Student T-tests were performed with cKO and Cre-negative controls to determine significance ($p<0.05$) for each metric.

Osteocyte-targeted *Rapsn* cKO leads to site specific skeletal abnormalities .

Rapsyn clusters cholinergic ion channels on the cell membrane, allowing for coordinated receptor/channel function and more potent responses. We repeated the same experiments performed above with *Chrna1* cKOs only now in *Rapsn* cKO mice (Figure 1B). To study growth and development, mice with *Rapsn* cKO had DEXA scans of the whole body, hind limbs, and lumbar spine overtime. We found that cKO mice for both sexes formed skeletons with bone mineral density (BMD) that were not altered compared to Cre-negative littermate controls (Figure 5A-F). We also evaluated tissue level differences using µCT analysis of the tibia. We observed decreases in cortical bone volume (-5.1%, Cort.BV, Figure 7A), cortical total volume (-8.3%, Cort.TV; Figure 7B), the total volume (-8.3% Tot.TV, Figure 7E) and bone mineral density (+1.3%, Cort.BMD; Figure 7F) for female *Rapsn*$^{\Delta Ocy/\Delta Ocy}$ mice with respect to *Rapsn*$^{+/+}$ controls. Male *Rapsn* $^{\Delta Ocy/\Delta Ocy}$ mice did not have any changes in the lumbar region (Figure 5 H-N) compared to Cre-negative controls. Male *Rapsn* $^{\Delta Ocy/\Delta Ocy}$ mice had increased bone volume density at the midshaft (+1.2%, MS.DenBV; Figure 7H) compared to Cre-negative littermate controls.

Osteocyte-targeted *Rapsn* cKO does not alter whole-bone level mechanical competence in femurs. We sought to determine if there would be differences to the whole bone mechanical properties following *Rapsn* cKO, and therefore dissected femurs from 16-18 week mice. Femurs from *Rapsn*$^{\Delta Ocy/\Delta Ocy}$ and Cre-negative littermate controls were subjected to monotonic loading to failure. Female mice did not show any differences in mechanical properties, whereas *Rapsn*$^{\Delta Ocy/\Delta Ocy}$ males only exhibited +10.9% higher ultimate force than controls (Figure 6J). After measuring tissue composition of a subset of femurs used for mechanical testing, we determined no changes to the mineral to matrix ratio, collagen maturity, or mineral crystallinity for cKO compared to Cre-negative controls (Figure 6I-J).

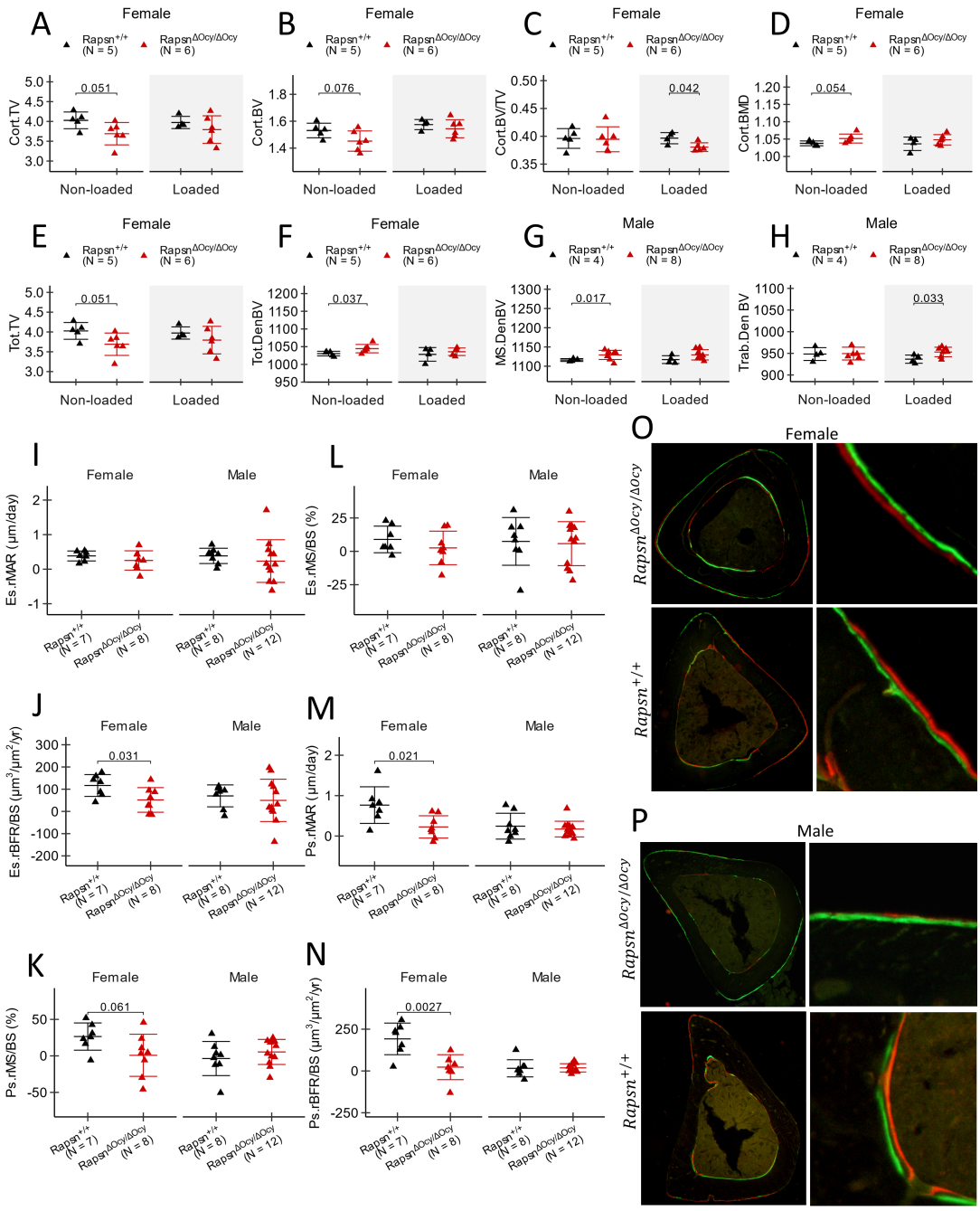

Fig. 7. *Rapsn* cKO impaired bone formation in response to mechanical load. Adult mice were subjected to tibial loading and bones dissected 12 days later. µCT of dissected tibia measured bone geometry for (I-L) females and (M-X) males to compare loaded limbs (shaded grey background) and non-loaded limbs (white background). Female *Rapsn* cKOs exhibited differences in trabecular phenotype and male *Rapsn* cKOs exhibited few differences. Fluorochrome labeling was used for osteoblast-derived indices of dynamic histomorphometry in (I-L) females and (O-S) males with relative metrics computed by subtracting non-loaded limbs from loaded limbs. Indices were computed for both the endosteal and periosteal surfaces. Female *Rapsn* cKOs exhibited reduced bone formation rates. Student T-tests were performed between cKOs and Cre-negative controls to determine significance (p<0.05). For µCT, groups within each loading regime (i.e. non-loaded and loaded) were compared.

Osteocyte-targeted *Rapsn* deletion impairs bone anabolic response to mechanical challenge.

To assess the impact of rapsyn on bone mechanotransduction, we studied tissue changes in response to *in vivo* loading. Mice received *in vivo* tibial loading to peak calibrated strain magnitudes of -2250με 3 times per week for 2 weeks. Post-mortem analyses of loaded and non-loaded tibia included CT and dynamic histomorphometry. Non-loaded tibiae from $Rapsn^{\Delta Ocy/\Delta Ocy}$ females exhibited deterioration in the metaphyseal cortex compared to Cre-negative littermate controls. Loading rescued this phenotype, returning all deficiencies back to baseline (Figure 7A-B, E, grey background). Loading also decreased bone volume over total compared to $Rapsn^{+/+}$ controls volume (-4.1%, Cort.BV/TV; Figure 7C). In male $Rapsn^{\Delta Ocy/\Delta Ocy}$ mice, loading caused increased bone volume density in the metaphyseal trabeculae (+1.8%, Trab.Den BV; Figure 7H). Relative dynamic histomorphom-

etry indices were assessed by subtracting non-loaded values from loaded limbs. *Rapsn*$^{\Delta Ocy/\Delta Ocy}$ females suffered from lower metabolic rates on the periosteum compared to Cre-negative littermate controls, with suppression of relative mineral apposition rate (Ps.rMAR) by -70.6%, relative mineralizing surface (Ps.rMS/BS) by -25.6%, and relative bone formation rate (Ps.rBFR) by -88.2% (Figure 7O). Females also had reduced endosteal relative bone formation rate (-55.7%, Es.rBRF; Figure 7K). In males, *Rapsn*$^{\Delta Ocy/\Delta Ocy}$ mice showed no differences compared to Cre-negative littermate controls.

3D Characterization of Skeletal Innervation reveals Cavities where Nerves Penetrate the Cortex and Enter the Marrow Space. Imaging of tissue cleared third metatarsals was performed using light sheet microscopy. Combining tissue clearing with microscopy would allowed us to map large nerve fibers of different functionality: VAChT positively stained bodies to indicate cholinergic nerve fibers and TH positively stained bodies to indicate adrenergic nerve fibers in bone (Figure 8A-D). Nerves were found to penetrate the cortical shell at different sites along the metatarsal, including the distal (Figure 8B), medial (Figure 8C, and proximal (Figure 8D) ends. Tracing of cholinergic and adrenergic positively stained bodies was performed in metatarsals from each cKO strain and sex (Figure 8E-H), however only *Chrna1* cKO males were found to have reductions in maximum number of branch points as well as average segment straightness (Figure 8F) compared to Cre-negative controls.

Discussion

Here, we determined that cholinergic signaling through *Chrna1* and *Rapsn* associated nAChRs in osteocytes were slightly impactful for bone growth and development and also important for mechanoadaptation. Our motivation stemmed from the known impact of cholinergic signaling/therapeutics on fracture risk (43, 44) and bone mass (45, 46). In the work reported here, we follow up prior evidence from others that osteocytes respond to ACh (67) and express genes for nAChRs (47) that are differentially expressed after mechanical loading (53) with our own data verifying osteocytes as direct cholinergic targets *in vivo*.

We achieved conditional osteocyte-targeted deletion of *Chrna1* and *Rapsn*, which caused impairments to bone structure and bone anabolism in a sexually dimorphic manner. Female *Chrna1* cKOs showed deteriorated microarchitecture at the tibial metaphysis while female *Rapsn* cKO showed reductions to the cortex. Male *Chrna1* cKO mice suffered from smaller cortical shells at the midshaft in the tibia with increased ductility and toughness in femurs. Broad phenotypic changes in BMD during skeletal development were not observed. AChE levels peak in early development to guide endochondral ossification before drastically declining, maintaining low levels for the majority of life (68). Further investigation including earlier ages (<4 weeks) is needed to interrogate periods of elevated developmental cholinergic signaling. Reduced ACh and increased AChE levels may occur in the elderly and are both associated with age-related disease such as dementia. Thus, how cholinergic tone impacts bone through in aging is also an important line of study that needs to be followed.

Our second goal was to assess the tissue level response to mechanical loading. This experiment revealed that cKO driven deficiencies in the cancellous (female *Chrna1*$^{\Delta Ocy/\Delta Ocy}$) and compact (female *Rapsn*$^{\Delta Ocy/\Delta Ocy}$) bone could be rescued with tibial loading. Counterintuitively, *Rapsn*$^{\Delta Ocy/\Delta Ocy}$ females also had suppressed bone formation and mineral apposition rate, indicating an alternative recovery mechanism. Since the present study only measured osteoblast-derived indices, we cannot disregard the possibility that osteoclasts driving bone resorption are involved. ACh stimulation of MLO-Y4 cells increases the RANKL/OPG expression ratio 60-fold (67). Adding either mecamylamine, a non-competitive antagonist that inhibits all known nAChRs, or d-Tubocurarine, a non-depolarizing competitive antagonist that acts particularly on muscle nAChRs, ablates the response. Pyridostigmine, an AChE inhibitor that is not blood brain barrier permeable (i.e. solely peripheral acting), increases RANKL/OPG serum levels and reduces femoral bone volume (69). Thus, nAChR activation on osteocytes may produce signals for osteoclast activity, implying *Rapsn* cKO could inhibit bone resorption. In contrast to females, any reductions in the *Chrna1*$^{\Delta Ocy/\Delta Ocy}$ males remained significantly lower even with loading, indicating distinct ACh mediated bone metabolism regulation.

Sex differences from cKOs imply different roles for ACh, corroborating further evidence that cholinergic signaling has a greater impact in females than in males. The negative bone measures associated with Alzhiemer's, which in general reduces ACh levels in the body, are mostly found in women and not men (40–42, 70). In general, women are more susceptible to both post-menopausal bone loss and dementia. Given the increased risk of osteoporosis with estrogen depletion, it may be possible that estrogen is also playing a role in the cholinergic regulation of bone, as indicated from the results in this study, although further investigation is necessary. Our results corroborate other studies on nAChRs in bone that found sex differences. For example, α7 global knockout does not produce changes in males (71), but in females results in increased cortical geometry and reduced calcium content (72) as well as reductions in osteoclast count, RANKL serum levels, and increases to OPG serum levels (73). α9 global knockout in females leads to an increased number of apoptotic osteocytes (74). α2 global knockouts in female suffer from reduced trabecular bone volume and increased osteoclast count as well as resorption activity (45). Additional studies are needed to interrogate the potential for these additional subunits as osteocyte mechanotransduction regulators, and also as sex-specific regulators of bone mechanotransduction more broadly.

An important consideration includes the spatial patterning of neurons in the bone and their relation to bone cells. Using a novel tissue clearing protocol produced by our lab and collaborators, we have successfully tissues cleared whole-mount

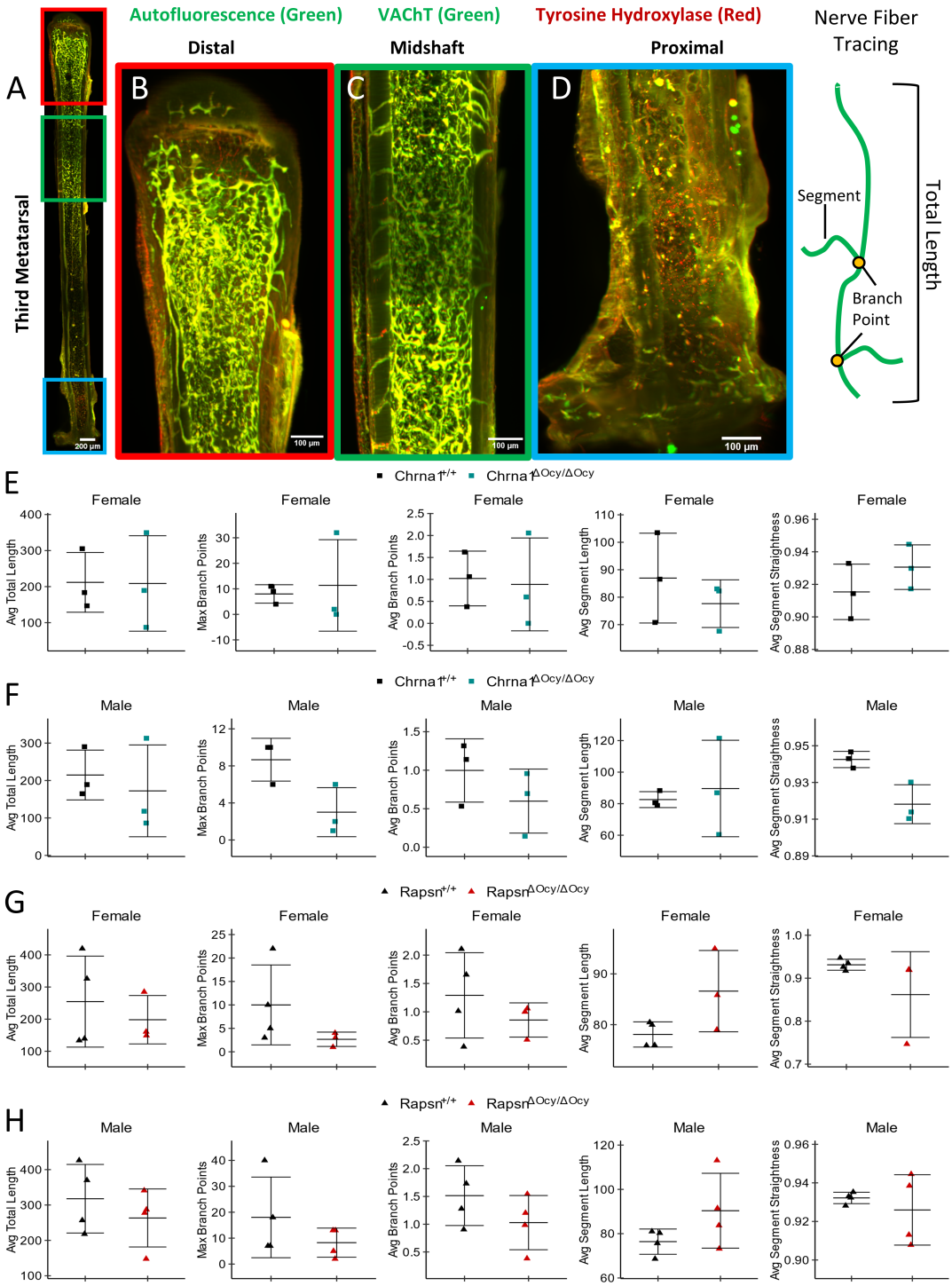

Fig. 8. 3D Reconstruction of Skeletal Innervation from Light Sheet Microscopy. Third metatarsals were dissected from perfused mice and used for whole-mount tissue clearing and light sheet microscopy. Immunofluorescent staining for VAChT and TH was performed to produce 3D reconstructions of bones for characterization of skeletal innervation manually traced in Imaris. (A) Whole Metatarsal with close-ups at the (B) Distal, (C) Midshaft and (D) Proximal ends. Filament tracing in Imaris allowed for characterization using global metrics for each metatarsal, including average total length, max branch points, average branch points, average segment length, and average segment straightness for *Chrna1* (E) females and (F) males and *Rapsn* (G) females and (H) males. Student T-tests were performed between cKOs and Cre-negative controls to determine significance ($p<0.05$).

bones for 3D characterization of skeletal innervation. Cavities that acted as entry points into the marrow space for large nerve fibers were found to penetrate various regions of the cortical shell, with higher densities at the distal and proximal ends compared to the midshaft. The embedded position of these nerves suggests direct communication with osteocytes. One meaningful limitation to the current work is that only larger positively stained bodies are currently resolved. Future work will include larger load-bearing long-bones, such as the femur and tibia, and may also be expanded with two-

photon microscopy for the visualization of smaller nerve bodies, such as soma and axons.

Distinct pathways in cholinergic disruption may explain the different phenotypes exhibited from the two cKOs. We expect the osteocyte cholinergic receptor has a similar conformation as muscle nAChRs, based on the component gene expression (47). These structures are heteropentameric with the stoichiometry $(\alpha 1)_2\beta 1\gamma\delta$ (75). The α1-ε and α1-δ interfaces act as the binding sites for ACh, and deletion of key hydrophobic regions to α1 abolish receptor function; thus, α1 knockout in osteocytes presumably inhibits nAChR function, although there may be stoichiometries substituting the α subunit that are we are not aware of that provide altered/limited receptor function. Rapsyn deletion permits healthy individual receptor formation while reducing overall signaling potency on account of increased receptor mobility. Rapsyn is also known to assist in faster recovery rates (76), meaning deletion may result in decreased signaling efficiency and effect.

Chrna1 and *Rapsn* cKOs are unlikely to ablate cholinergic signaling entirely in the osteocyte, as other cholinergic receptors may be present (47, 67). Despite this occurance, we have seen definitive evidence that osteocyte cholinergic receptors are important for bone development and response to mechanical challenge. This study did not trace the cholinergic source. This is important because ACh may be derived from a neuronal (e.g. parasympathetic/sympathetic nervous system (45, 46)) or non-neuronal (e.g. osteoblasts/bone lining cells (46, 48)) source, which have various biological implications and may also influence future therapeutic strategies . An important advance demonstrated in this study was the use of targeted genetic modification of ACh signaling in osteocytes specifically, rather than systemic pharmacological disruption or global knockout. Thus, we able to show that ACh signaling to osteocytes directly impacts bone morphology and mechanoadaptation. This indicates an important new signaling axis, potentially implicating autonomic nervous system modulation of osteocyte activity.

With this work, we introduce a novel signaling pathway that suggests ACh can act on osteocytes *in vivo* to alter bone mass. Given the escalating prevalence of osteoporosis, investigating osteocyte-based therapeutics is a critical next step to advancing treatments beyond what is currently possible. Cholinergic neuromodulators such as AChE inhibitors are already commonly used to treat neurodegenerative diseases such as Alzheimer's and have been gaining traction as potential therapeutics for bone diseases such as osteoporosis. To get closer to clinical translation, there is still a much-needed understanding of how cholinergic signaling impacts bone (specifically in osteocytes), and how this effect alters bone mechanotransduction. Our research is helping to elucidate the mechanism of cholinergic signaling in osteocyte mechanobiology and suggests a new signaling axis between brain and bone with far reaching implications in bone biology that may be vital to treat bone disease.

ACKNOWLEDGEMENTS

We thank Karly Hooper for maintaining mouse colonies for use in these experiments, along with the entire CARE staff in Weill Hall. We thank the Donnelly Lab in the Materials Science and Engineering Department at Cornell University for assistance with FTIR collection. We also thank Dan Horan, April Hoggat, and Alexander Robling at Indiana University School of Medicine for the founding breeders and assistance with microcomputed tomography scans. Finally, we thank Damien Laudier for histological guidance for the bone clearing protocol reported here. This work was supported by the Department of Biomedical Engineering at Cornell University, the Mong Family Foundation at Cornell University, and the Ford Foundation by the National Academies of Sciences, Medicine, and Engineering, NIH S10OD023466 for the light sheet microscope at the Cornell BRC, and NIH NIAMS .

Bibliography

1. Frost, H. M. Bone's mechanostat: A 2003 update. Anat. Rec. 275A, 1081–1101 (2003).
2. Frost, H. M. The Regional Acceleratory Phenomenon: A Review. Henry Ford Hospital Medical Journal 31, 3–9 (1983).
3. Frost, H. M. Bone As A Physiological Tool. Henry Ford Hospital Medical Bulletin 14, 63–70 (1966).
4. Rubin, C. T. Lanyon, L. E. Dynamic strain similarity in vertebrates; an alternative to allometric limb bone scaling. Journal of Theoretical Biology 107, 321–327 (1984).
5. Rubin, C. T. Lanyon, L. E. Regulation of bone mass by mechanical strain magnitude. Calcif Tissue Int 37, 411–417 (1985).
6. Sozen, T., Ozisik, L. Calik Basaran, N. An overview and management of osteoporosis. Eur J Rheumatol 4, 46–56 (2017).
7. Reginster, J.-Y. Burlet, N. Osteoporosis: A still increasing prevalence. Bone 38, 4–9 (2006).
8. Lanyon, L. E. Osteocytes, strain detection, bone modeling and remodeling. Calcif Tissue Int 53, S102–S107 (1993).
9. Schaffler, M. B., Cheung, W.-Y., Majeska, R. Kennedy, O. Osteocytes: Master Orchestrators of Bone. Calcif Tissue Int 94, 5–24 (2014).
10. Bonewald, L. F. Johnson, M. L. Osteocytes, mechanosensing and Wnt signaling. Bone 42, 606–615 (2008).
11. Kamioka, H. et al. Primary Cultures of Chick Osteocytes Retain Functional Gap Junctions between Osteocytes and between Osteocytes and Osteoblasts. Microsc Microanal 13, 108–117 (2007).
12. Cherian, P. P. et al. Mechanical Strain Opens Connexin 43 Hemichannels in Osteocytes: A Novel Mechanism for the Release of Prostaglandin. Molecular Biology of the Cell 16, (2005).
13. Clapham, D. E. Calcium Signaling. Cell 131, 1047–1058 (2007).
14. Bootman, M. D. Calcium Signaling. Cold Spring Harbor Perspectives in Biology 4, a011171–a011171 (2012).
15. Lu, X. L., Huo, B., Chiang, V. Guo, X. E. Osteocytic network is more responsive in calcium signaling than osteoblastic network under fluid flow. J Bone Miner Res 27, 563–574 (2012).
16. Lu, X. L., Huo, B., Park, M. Guo, X. E. Calcium response in osteocytic networks under steady and oscillatory fluid flow. Bone 51, 466–473 (2012).
17. Xu, H. et al. Oscillatory fluid flow elicits changes in morphology, cytoskeleton and integrin-associated molecules in MLO-Y4 cells, but not in MC3T3-E1 cells. Biol. Res. 45, 163–169 (2012).
18. Bakker, A. D., Soejima, K., Klein-Nulend, J. Burger, E. H. The production of nitric oxide and prostaglandin E2 by primary bone cells is shear stress dependent. Journal of Biomechanics 34, 671–677 (2001).
19. Klein-Nulend, J. et al. Sensitivity of osteocytes to biomechanical stress in vitro. FASEB j. 9, 441–445 (1995).
20. Hung, C. T., Allen, F. D., Pollack, S. R. Brighton, C. T. Intracellular Ca2+ stores and extracellular Ca2+ are required in the real-time Ca2+ response of bone cells experiencing fluid flow. Journal of Biomechanics 29, 1411–1417 (1996).
21. Ajubi, N. E. et al. Pulsating Fluid Flow Increases Prostaglandin Production by Cultured Chicken Osteocytes—A Cytoskeleton-Dependent Process. Biochemical and Biophysical Research Communications 225, 62–68 (1996).
22. Weinbaum, S., Cowin, S. C. Zeng, Y. A model for the excitation of osteocytes by mechanical loading-induced bone fluid shear stresses. Journal of Biomechanics 27, 339–360 (1994).
23. Jacobs, C. R., Temiyasathit, S. Castillo, A. B. Osteocyte Mechanobiology and Pericellular Mechanics. Annu. Rev. Biomed. Eng. 12, 369–400 (2010).
24. Zaman, G. et al. Mechanical Strain Stimulates Nitric Oxide Production by Rapid Activation of Endothelial Nitric Oxide Synthase in Osteocytes. J of Bone Mineral Res 14, 1123–1131 (1999).
25. Mikuni-Takagaki, Y., Suzuki, Y., Kawase, T. Saito, S. Distinct responses of different populations of bone cells to mechanical stress. Endocrinology 137, 2028–2035 (1996).
26. Rawlinson, S. C. F., Mosley, J. R., Suswillo, R. F. L., Pitsillides, A. A. Lanyon, L. E. Calvarial and limb bone cells in organ and monolayer culture do not show the same early responses to dynamic mechanical strain. J Bone Miner Res 10, 1225–1232 (2009).
27. Nagatomi, J., Arulanandam, B. P., Metzger, D. W., Meunier, A. Bizios, R. Frequency- and Duration-Dependent Effects of Cyclic Pressure on Select Bone Cell Functions. Tissue Engineering 7, 717–728 (2001).
28. Takai, E., Mauck, R. L., Hung, C. T. Guo, X. E. Osteocyte Viability and Regulation of Osteoblast Function in a 3D Trabecular Bone Explant Under Dynamic Hydrostatic Pressure. J Bone Miner Res 19, 1403–1410 (2004).
29. Gardinier, J. D., Majumdar, S., Duncan, R. L. Wang, L. Cyclic Hydraulic Pressure and Fluid Flow Differentially Modulate Cytoskeleton Re-Organization in MC3T3 Osteoblasts. Cel. Mol. Bioeng. 2, 133–143 (2009).
30. Kamel, M. A., Picconi, J. L., Lara-Castillo, N. Johnson, M. L. Activation of β-catenin signaling in MLO-Y4 osteocytic cells versus 2T3 osteoblastic cells by fluid flow shear stress and PGE2: Implications for the study of mechanosensation in bone. Bone 47, 872–881 (2010).
31. Case, N. et al. β-Catenin Levels Influence Rapid Mechanical Responses in Osteoblasts. Journal of Biological Chemistry 283, 29196–29205 (2008).

32. Kramer, I. et al. Osteocyte Wnt/β-Catenin Signaling Is Required for Normal Bone Homeostasis. Molecular and Cellular Biology 30, 3071–3085 (2010).
33. Plotkin, L. I. et al. Inhibition of Osteocyte Apoptosis Prevents the Increase in Osteocytic Receptor Activator of Nuclear Factor κB Ligand (RANKL) but Does Not Stop Bone Resorption or the Loss of Bone Induced by Unloading. Journal of Biological Chemistry 290, 18934–18942 (2015).
34. Cabahug-Zuckerman, P. et al. Osteocyte Apoptosis Caused by Hindlimb Unloading is Required to Trigger Osteocyte RANKL Production and Subsequent Resorption of Cortical and Trabecular Bone in Mice Femurs. J of Bone Mineral Res 31, 1356–1365 (2016).
35. Baron, R. Rawadi, G. Targeting the Wnt/β-Catenin Pathway to Regulate Bone Formation in the Adult Skeleton. Endocrinology 148, 2635–2643 (2007).
36. Arnsdorf, E. J., Tummala, P. Jacobs, C. R. Non-Canonical Wnt Signaling and N-Cadherin Related β-Catenin Signaling Play a Role in Mechanically Induced Osteogenic Cell Fate. PLoS ONE 4, e5388 (2009).
37. Robling, A. G. et al. Mechanical Stimulation of Bone in Vivo Reduces Osteocyte Expression of Sost/Sclerostin. Journal of Biological Chemistry 283, 5866–5875 (2008).
38. Keller, H. Kneissel, M. SOST is a target gene for PTH in bone. Bone 37, 148–158 (2005).
39. Kitase, Y. et al. Mechanical induction of PGE2 in osteocytes blocks glucocorticoid-induced apoptosis through both the β-catenin and PKA pathways. J Bone Miner Res 25, 2657–2668 (2010).
40. Tan, Z. S. et al. Bone Mineral Density and the Risk of Alzheimer Disease. Arch Neurol 62, 107 (2005).
41. Tsai, C.-H. et al. Fracture as an Independent Risk Factor of Dementia: A Nationwide Population-Based Cohort Study. Medicine 93, e188 (2014).
42. Chang, K.-H. et al. Increased risk of dementia in patients with osteoporosis: a population-based retrospective cohort analysis. AGE 36, 967–975 (2014).
43. Tamimi, I. et al. Acetylcholinesterase inhibitors and the risk of hip fracture in Alzheimer's disease patients: A case-control study. J Bone Miner Res 27, 1518–1527 (2012).
44. Eimar, H. et al. Acetylcholinesterase inhibitors and healing of hip fracture in Alzheimer's disease patients: a retrospective cohort study. 13, 454–463 (2013).
45. Bajayo, A. et al. Skeletal parasympathetic innervation communicates central IL-1 signals regulating bone mass accrual. Proc Natl Acad Sci USA 109, 15455–15460 (2012).
46. Gadomski, S. et al. A cholinergic neuroskeletal interface promotes bone formation during postnatal growth and exercise. Cell Stem Cell 29, 528-544.e9 (2022).
47. Paic, F. et al. Identification of differentially expressed genes between osteoblasts and osteocytes. Bone 45, 682–692 (2009).
48. En-Nosse, M. et al. Expression of non-neuronal cholinergic system in osteoblast-like cells and its involvement in osteogenesis. Cell Tissue Res 338, 203–215 (2009).
49. Role, L. W. Berg, D. K. Nicotinic Receptors in the Development and Modulation of CNS Synapses. Neuron 16, 1077–1085 (1996).
50. Fucile, S. Ca2+ permeability of nicotinic acetylcholine receptors. Cell Calcium 35, 1–8 (2004).
51. Karlin, A. Structure of nicotinic acetylcholine receptors. Current Opinion in Neurobiology 3, 299–309 (1993).
52. Sine, S. M. End-Plate Acetylcholine Receptor: Structure, Mechanism, Pharmacology, and Disease. Physiological Reviews 92, 1189–1234 (2012).
53. Mantila Roosa, S. M., Liu, Y. Turner, C. H. Gene expression patterns in bone following mechanical loading. J Bone Miner Res 26, 100–112 (2011).
54. Sato, T. et al. Functional role of acetylcholine and the expression of cholinergic receptors and components in osteoblasts. FEBS Letters 584, 817–824 (2010).
55. Pires-Oliveira, M., Moen, D. Akaaboune, M. Dynamics of Nicotinic Acetylcholine Receptors and Receptor-Associated Proteins at the Vertebrate Neuromuscular Junction. CAR 10, 631–641 (2013).
56. Ramarao, M. K. Cohen, J. B. Mechanism of nicotinic acetylcholine receptor cluster formation by rapsyn. Proc. Natl. Acad. Sci. U.S.A. 95, 4007–4012 (1998).
57. Ramarao, M. K., Bianchetta, M. J., Lanken, J. Cohen, J. B. Role of Rapsyn Tetratricopeptide Repeat and Coiled-coil Domains in Self-association and Nicotinic Acetylcholine Receptor Clustering. Journal of Biological Chemistry 276, 7475–7483 (2001).
58. An, M. C. et al. Acetylcholine negatively regulates development of the neuromuscular junction through distinct cellular mechanisms. Proc. Natl. Acad. Sci. U.S.A. 107, 10702–10707 (2010).
59. Gautam, M. et al. Failure of postsynaptic specialization to develop at neuromuscular junctions of rapsyn-deficient mice. Nature 377, 232–236 (1995).
60. Raymond, C. S. Soriano, P. High-Efficiency FLP and ΦC31 Site-Specific Recombination in Mammalian Cells. PLoS ONE 2, e162 (2007).
61. Lu, Y. et al. DMP1-targeted Cre Expression in Odontoblasts and Osteocytes. J Dent Res 86, 320–325 (2007).
62. Niziolek, P. J., Warman, M. L. Robling, A. G. Mechanotransduction in bone tissue: The A214V and G171V mutations in Lrp5 enhance load-induced osteogenesis in a surface-selective manner. Bone 51, 459–465 (2012).
63. Dempster, D. W. et al. Standardized nomenclature, symbols, and units for bone histomorphometry: A 2012 update of the report of the ASBMR Histomorphometry Nomenclature Committee. J Bone Miner Res 28, 2–17 (2013).
64. Allen, M. R. Burr, D. B. Techniques in Histomorphometry. in Basic and Applied Bone Biology 131–148 (Elsevier, 2014). doi:10.1016/B978-0-12-416015-6.00007-1.
65. Jepsen, K. J., Silva, M. J., Vashishth, D., Guo, X. E. van der Meulen, M. C. Establishing Biomechanical Mechanisms in Mouse Models: Practical Guidelines for Systematically Evaluating Phenotypic Changes in the Diaphyses of Long Bones. J Bone Miner Res 30, 951–966 (2015).
66. Hunt, H. B. et al. Altered Tissue Composition, Microarchitecture, and Mechanical Performance in Cancellous Bone From Men With Type 2 Diabetes Mellitus. Journal of Bone and Mineral Research 34, 1191–1206 (2019).
67. Ma, Y. et al. Acetylcholine affects osteocytic MLO-Y4 cells via acetylcholine receptors. Molecular and Cellular Endocrinology 384, 155–164 (2014).
68. Luo, X., Lauwers, M., Layer, P. G. Wen, C. Non-neuronal Role of Acetylcholinesterase in Bone Development and Degeneration. Front. Cell Dev. Biol. 8, 620543 (2021).
69. Ma, Y. Elefteriou, F. Brain-Derived Acetylcholine Maintains Peak Bone Mass in Adult Female Mice. J Bone Miner Res 35, 1562–1571 (2020).
70. Bliuc, D. et al. Cognitive decline is associated with an accelerated rate of bone loss and increased fracture risk in women: a prospective study from the Canadian Multicentre Osteoporosis Study. J of Bone Mineral Res 36, 2106–2115 (2021).
71. Kliemann, K. et al. Quantitative analyses of bone composition in acetylcholine receptor M3R and alpha7 knockout mice. Life Sciences 91, 997–1002 (2012).
72. Lips, K. S. et al. Small changes in bone structure of female α7 nicotinic acetylcholine receptor knockout mice. BMC Musculoskelet Disord 16, 5 (2015).
73. Mito, K. et al. The nicotinic acetylcholine receptor α7 subunit is an essential negative regulator of bone mass. Sci Rep 7, 45597 (2017).
74. Baumann, L. et al. Deletion of nicotinic acetylcholine receptor alpha9 in mice resulted in altered bone structure. Bone 120, 285–296 (2019).
75. Mishina, M. et al. Molecular distinction between fetal and adult forms of muscle acetylcholine receptor. Nature 321, 406–411 (1986).
76. Cetin, H. et al. Rapsyn facilitates recovery from desensitization in fetal and adult acetylcholine receptors expressed in a muscle cell line. J Physiol 597, 3713–3725 (2019).
77. Bouxsein, M. L. et al. Guidelines for assessment of bone microstructure in rodents using micro-computed tomography. J Bone Miner Res 25, 1468–1486 (2010).
78. Lewis, K. J. et al. Osteocyte calcium signals encode strain magnitude and loading frequency in vivo. Proc. Natl. Acad. Sci. U.S.A. 114, 11775–11780 (2017).